Random FM Waveforms Jointly Optimized for Delay-Doppler Ambiguity Shaping

David G. Felton, Jonathan W. Owen, Shannon D. Blunt,
Radar Systems Lab (RSL), University of Kansas, Lawrence, KS

Abstract – Waveform agility introduces additional degrees of freedom to achieve distinct operational objectives. However, pulse-to-pulse diversity does come at the expense of range sidelobe modulation (RSM), which may mask small targets in proximity to large clutter returns. Sophisticated waveform design or receive processing techniques can improve detection capabilities by incorporating prior or assumed knowledge. Here, we consider a waveform design approach that jointly optimizes a set of random FM waveforms to suppress RSM within a specified region of the delay-Doppler response otherwise known as the point-spread function. This approach likewise provides a complementary condition that is chosen for a region of delay and Doppler. Joint optimization of waveform sets also introduces the prospect of a sense-and-notch (in delay-Doppler) cognitive capability.

Keywords*– *random frequency modulation (RFM), complementary waveforms, moving target indication, pulse agility, cognitive radar

I. Introduction

With the introduction of arbitrary waveform generation (AWG) capabilities, traditional frequency modulated (FM) waveform design comprising linear FM (LFM), hyperbolic FM (HFM) [1], and nonlinear FM (NLFM) [2], has expanded to include a variety of forms of random FM (RFM) waveforms [3]. The RFM notion greatly increases design degrees of freedom while maintaining a physically realizable structure that is amenable to high-power transmitters. Further, advances in high-performance processing allow for real-time design of modest time-bandwidth (*TB*) product waveforms that have complex modulation structures. This increased complexity is accompanied by a new realm of design potential, particularly for waveform sets collectively constructed for a coherent processing interval (CPI).

In radar applications employing unique waveforms on a pulse-to-pulse basis (i.e. pulse/waveform agility), new capabilities can emerge due to expanded dimensionality (see [4]). Such uniqueness may include waveforms operating at different center frequencies [5], pulse widths [6], or phase/frequency modulation [3]. Of course, any radar operation is limited by the waveform *TB* aggregated over the CPI, receive signal-to-noise ratio (SNR), and estimation error in the form of correlation sidelobes. Pulse agility also introduces estimation error known as range-sidelobe modulation (RSM), resulting from inter-pulse correlation sidelobe dissimilarity that produces phase/amplitude variation across slow-time. While this effect is known to degrade standard clutter cancellation [7], various non-adaptive receive processing algorithms have been proposed to alleviate the issue including least-squares mismatched filtering [8], complementary-on-receive mismatch filtering [9], and joint range-Doppler clutter cancellation approaches [10].

The impact of RSM can likewise be partially mitigated through waveform design by shaping the anticipated matched filter response (characterized by the autocorrelation) [11-14]. For instance, waveform sidelobe minimization reduces RSM but does not eliminate it [11]. In [12], information about the illuminated scene is used to shape the waveform autocorrelation to improve subsequent scene estimation. Further, knowledge of scene interference can be incorporated into waveform design to maximize the signal-to-interference-plus-noise ratio (SINR), accounting for correlation and interference error [13, 14].

Here, the waveforms forming a CPI are jointly optimized to minimize RSM within an unambiguous delay-Doppler region. The designated delay-Doppler region may encompass the entire space between $\tau \in (-T_{\mathrm{PRI}}, T_{\mathrm{PRI}})$ and $f_{\mathrm{D}} \in (-f_{\mathrm{PRF}}/2, f_{\mathrm{PRF}}/2)$, for the uniform PRI denoted T_{PRI} and associated pulse repetition frequency (PRF) defined as $f_{\mathrm{PRF}} = 1/T_{\mathrm{PRI}}$. Alternatively, the available waveform degrees of freedom can be focused into a sub-region therein. Doing so provides the capability to better estimate a delay-Doppler region in the presence of expected large clutter, akin to [12], but here deterministically chosen and optimized in joint delay-Doppler. This optimization procedure is a natural extension of incorporating Doppler tolerance into complementary FM waveforms explored in [15]. While the intention of this work is to summarize the waveform design, further extension for use in conjunction with a cognitive engine warrants exploration [16, 17].

II. FM Signal Model

Frequency modulated (FM) waveforms possess two desirable characteristics: constant amplitude and continuous phase. These attributes are essential for high-power radar transmission to accomodate unavoidable distortions cause by amplification. Consider the unit amplitude FM waveform of pulse width T and time support $[0, T]$:

$$s(t) = e^{j\phi(t)}, \tag{1}$$

where $\phi(t)$ is an instantaneous phase function that varies over the duration of the pulse width. The first derivative of the instantaneous phase function

$$\omega(t) = \frac{\phi(t)}{dt} \tag{2}$$

represents the time-varying radial frequency that provides the FM structure. Discretizing $s(t)$ at some sampling frequency F_{s} provides the discretized representation

This work was supported by the Office of Naval Research under Contract #N00014-23-C-1053. DISTRIBUTION STATEMENT A. Approved for Public Release. The views expressed are those of the author and do not reflect the official policy or position of the Department of Defense or the U.S. Government. DCN# 2025-3-4-697.

$$\mathbf{s} = e^{j\boldsymbol{\phi}} = [s(0) \quad s(T_s) \quad \dots \quad s((M-1)T_s)]^T, \quad (3)$$

where $\boldsymbol{\phi} \in \mathbb{R}^{M\times 1}$ contains samples of $\phi(t)$ and $T_{\rm s} = 1/F_{\rm s}$ is the sample period. The waveform is often designed with a degree of "oversampling" relative to a meaningful bandwidth definition, thus enabling spectral containment. Often, the occupied bandwidth is measured in terms of an energy efficiency (e.g. 98% percent energy) or a threshold relative to peak energy (e.g. 6-dB bandwidth) [18]. Here, we use the Gabor/RMS bandwidth from [19], which is

$$\mathcal{B}^2 = \frac{1}{2\pi T}\int_{-\infty}^{\infty} \xi^2 |S(\xi)|^2 d\xi = \frac{1}{T}\int_{-\infty}^{\infty} \omega^2(t) dt \quad (4)$$

for ξ a radial frequency value, $S(\xi)$ the Fourier transform of $s(t)$ (scaled to preserve total energy), and the right-hand side of (4) is true due to the constant envelope of $s(t)$. Therefore, the RMS bandwidth is a weighted average of the power spectrum $|S(\xi)|^2$, with an equivalent temporal form expressed in terms of the waveform instantaneous frequencies. The relationship between instantaneous frequency and the accumulated RMS bandwidth is further developed in [20, 21]. An important distinction is emphasized upon sampling $\phi(t)$: spectral containment of $s(t)$ implies that the relative phase-change between adjacent samples of $\boldsymbol{\phi}$ is small (thus preventing $\omega(t)$ from becoming excessively large).

Here, the first-order polyphase-coded FM (PCFM) quasi-basis is selected, which has parameters representing instantaneous radial-frequencies that are imposed onto the waveform by a selected frequency shaping filter $g(t)$. The instantaneous frequency function of PCFM is [24]

$$\omega_{\rm PCFM}(t) = \sum_{n=0}^{N-1} \alpha_n\, g(t - nT_{\rm p}) \quad (5)$$

where $T_{\rm p} = T/N$ is the PCFM parameter interval (representing the "on-time" of each parameter) such that the instantaneous phase function becomes

$$\phi_{\rm PCFM}(t) = \sum_{n=0}^{N-1} \alpha_n\, b(t - nT_{\rm p}) \quad (6)$$

where

$$b(t) = \int_0^t g(u) du\,. \quad (7)$$

This transformation explicitly limits the instantaneous phase transition across parameter sub-intervals, which implicitly imposes a degree of spectral containment. Here, the frequency-shaping filter is chosen to be rectangular over $[0, T_{\rm p}]$ and scaled by $1/T_{\rm p}$ to integrate to unity. The phase $\phi_{\rm PCFM}(t)$ is consequently shaped by a linear ramp

$$b(t) = \begin{cases} 0 & t < 0 \\ t/T_{\rm p} & 0 \le t \le T_{\rm p}. \\ 1 & T_{\rm p} < t \end{cases} \quad (8)$$

The PCFM transform, when discretized, can be represented via the matrix-vector form

$$\boldsymbol{\phi} = \mathbf{B}\mathbf{x}, \quad (9)$$

where the n^{th} column of $\mathbf{B} \in \mathbb{R}^{M\times N}$ is a discretized version of $b(t - nT_{\rm p})$, and $\mathbf{x} = [\alpha_0 \quad \cdots \quad \alpha_{N-1}]^T$ is the PCFM parameter vector that contains instantaneous radial-frequency values.

For first-order PCFM with a rectangular shaping filter, it can be shown that the RMS bandwidth in (4) simplifies to

$$\mathcal{B}^2 = \frac{1}{T}\int_0^T \omega_{\rm PCFM}^2(t) dt = \frac{N}{T^2}\sum_{n=0}^{N-1} \alpha_n^2 = \frac{N}{T^2}\|\mathbf{x}\|_2^2\,, \quad (10)$$

which is now a function of only the PCFM parameters, and for $\|\cdot\|_2$ the Euclidean norm.

By the original definition of PCFM, all parameters α_n must have a magnitude $|\alpha_n| \le \pi$. This requirement subsequently enforces that the maximum phase transition be $\pi N/M$ so N approximates the time-bandwidth product TB. A bounded activation function is a simple way to meet this requirement. Consequently, consider the bounding function

$$\mathbf{x} = \frac{M}{N}\Delta_\phi \cos\tilde{\mathbf{x}} \quad (11)$$

as a simple means to limit the sample-to-sample phase transition, where Δ_ϕ represents the maximum permittable value, thereby now effectively setting TB. This definition likewise subsumes the previously explored "over-coded" and "over-phased" PCFM form [25] that increases the number of quasi-basis functions and the maximum permittable phase change, respectively, each uniquely impacting the waveform design space. Special care should be taken when allowing the maximum permittable phase transition to extend beyond the originally set limit of $\pi N/M$ (i.e., over-phasing) which inevitably inflates the waveform bandwidth $\mathcal{B}$.

III. Pulse-Doppler Performance Metrics

For standard pulse compression with the matched filter, a waveform's autocorrelation provides the expected delay-response from a single point scatterer as

$$r(\tau) = \int_{-\infty}^{\infty} s(t)s^*(t-\tau)dt\,. \quad (12)$$

Autocorrelation sidelobes are a form of self-interference that obstructs detectability of small scatterers in the presence of large scatterers. Sidelobes are typically measured by the integrated sidelobe level (ISL) and peak sidelobe level (PSL). The former captures the energy ratio between the integrated sidelobes and mainlobe, while the latter captures the energy ratio of the peak sidelobe to the mainlobe peak. Both are subsumed by the Generalized-ISL metric defined as [26]

$$\text{GISL} = \left(\frac{\int_{\Omega_{\rm SL}} |r(\tau)|^{\wp}}{\int_{\Omega_{\rm ML}} |r(\tau)|^{\wp}}\right)^{2/\wp} \quad (13)$$

where $\wp = 2$ denotes ISL and PSL corresponds to $\wp \to \infty$, and with $\Omega_{\rm SL}$ the delay values of the sidelobes region and $\Omega_{\rm ML}$ the delay interval of the mainlobe. The specified $\Omega_{\rm ML}$ establishes an implicit degree of spectral containment since bandwidth is inversely proportional to mainlobe width [27]. Discretization of the autocorrelation is achieved through the Fourier relationship with power spectral density (PSD) via

$$\mathbf{r} = \mathbf{A}^H |\tilde{\mathbf{A}}\mathbf{s}|^2, \quad (14)$$

where $\tilde{\mathbf{A}} \in \mathbb{C}^{2M-1\times M}$ is a truncated (or zero-padded) version of DFT matrix $\mathbf{A} \in \mathbb{C}^{2M-1\times 2M-1}$, which can be efficiently computed via FFT. Thus, the discretized GISL is

$$\mathrm{GISL} = \frac{\|\mathbf{w}_{\mathrm{SL}} \odot \mathbf{r}\|_{\wp}^2}{\|\mathbf{w}_{\mathrm{ML}} \odot \mathbf{r}\|_{\wp}^2} \tag{15}$$

for $\mathbf{w}_{\mathrm{SL}}, \mathbf{w}_{\mathrm{ML}} \in \mathbb{R}^{2M-1\times 1}$ binary valued sidelobe and mainlobe selector vectors, and $\|\cdot\|_{\wp}$ is the $\wp$-norm.

Optimization on a per-waveform basis, via power spectrum or autocorrelation shaping [3, 11], can minimize RSM that arises for nonrepeating waveforms – but never completely eliminates sidelobes due to a conservation of ambiguity [28]. Standard pulse-Doppler processing applies the matched filter in fast-time and Doppler estimation in slow-time via the Fourier transform, resulting in a "point-spread" function (PSF)

$$\Psi(\tau,\theta) = \sum_{p=0}^{P-1} \int_{-\infty}^{\infty} s_p(t) s_p^*(t+\tau) e^{-jp\theta} dt \tag{16}$$

in which $s_p(t)$ represents the p^{th} pulse (of P) and θ is a normalized Doppler value within a 2π span. The PSF represents the response from a single stationary point scatterer (i.e., the impulse response of the CPI) as a function of delay and Doppler [29]. Under a "stop and hop" assumption, the GISL definition for delay-only assessment can be extended to delay-Doppler through consideration of the PSF, expressed as

$$J(\Omega_{\mathrm{SL}};\wp) = \left(\frac{\iint_{\Omega_{\mathrm{SL}}} |\Psi(\tau,\theta)|^{\wp} d\tau d\theta}{\iint_{\Omega_{\mathrm{ML}}} |\Psi(\tau,\theta)|^{\wp} d\tau d\theta}\right)^{2/\wp}, \tag{17}$$

which realizes a two-dimensional measure according to specified delay-Doppler sidelobe region Ω_{SL} and fixed mainlobe region Ω_{ML}. Now collect the sequence of P PCFM waveforms within a CPI as

$$\mathbf{S} = e^{j\mathbf{BX}} = [\mathbf{s}_0 \quad \cdots \quad \mathbf{s}_{P-1}], \tag{18}$$

where $\mathbf{s}_p$ is parameterized by $\mathbf{x}_p$ that is the p^{th} column of PCFM parameter matrix $\mathbf{X}$. Discretization of the PSF yields

$$\mathbf{\Psi} = \mathbf{A}^H \left|\tilde{\mathbf{A}}\mathbf{S}\right|^2 \mathbf{F}, \tag{19}$$

where $\mathbf{F} \in \mathbb{C}^{P\times U}$ is a zero-padded DFT matrix for Doppler processing, U is the number of discretized frequency points, and $U \geq 2P-1$ to realize sufficient Doppler visibility/granularity. The P-pulse discretized delay-Doppler GISL is subsequently expressed as

$$J(\Omega_{\mathrm{SL}};\wp) = \frac{\|\mathbf{W}_{\mathrm{SL}} \odot \mathbf{\Psi}\|_{\wp}^2}{\|\mathbf{W}_{\mathrm{ML}} \odot \mathbf{\Psi}\|_{\wp}^2} \tag{20}$$

for $\mathbf{W}_{\mathrm{SL}}, \mathbf{W}_{\mathrm{ML}} \in \mathbb{R}^{2M-1\times U}$ now binary-valued selector matrices for the delay-Doppler sidelobe and mainlobe regions, respectively.

IV. Waveform Optimiziation

Non-convex surfaces require iterative solutions to find local minima. Now consider the gradient matrix operator

$$\frac{\partial}{\partial \mathbf{X}} = [\nabla_{\mathbf{x}_0} \quad \cdots \quad \nabla_{\mathbf{x}_{P-1}}] \tag{21}$$

where

$$\nabla_{\mathbf{x}_p} = \left[\frac{\partial}{\partial \alpha_{p,0}} \quad \cdots \quad \frac{\partial}{\partial \alpha_{p,N-1}}\right]^T \tag{22}$$

is the gradient vector operator. Leveraging the discretized representations above, application of (22) to (21) yields the gradient matrix

$$\begin{aligned}\frac{\partial J}{\partial \tilde{\mathbf{X}}} &= -4J\frac{M}{N}\Delta_{\phi}\sin(\tilde{\mathbf{X}}) \odot \mathbf{B}^T \\ &\Im\{\mathbf{S}^* \odot \tilde{\mathbf{A}}^H[(\tilde{\mathbf{A}}\mathbf{S}) \odot \Re\{\mathbf{A}(\mathbf{W}_{\Delta} \odot |\mathbf{\Psi}|^{\wp-2} \odot \mathbf{\Psi})\mathbf{F}^H\}]\}\end{aligned} \tag{23}$$

where $\Re\{\cdot\}$, $\Im\{\cdot\}$ extract the real and imaginary components, $\tilde{\mathbf{X}}$ reflects the same parameter limitation from (11) and

$$\mathbf{W}_{\Delta} = \frac{\mathbf{W}_{\mathrm{SL}}}{\|\mathbf{W}_{\mathrm{SL}} \odot \mathbf{\Psi}\|_{\wp}^{\wp}} - \frac{\mathbf{W}_{\mathrm{ML}}}{\|\mathbf{W}_{\mathrm{ML}} \odot \mathbf{\Psi}\|_{\wp}^{\wp}}. \tag{24}$$

Each element of the waveform matrix $\mathbf{S}$ is updated via the gradient-descent parameter update

$$\tilde{\mathbf{X}}^{(i+1)} = \tilde{\mathbf{X}}^{(i)} + \mu^{(i)}\mathbf{D}^{(i)}, \tag{25}$$

where $\mathbf{D}^{(i)}$ is a descent search direction at the i^{th} iteration, and $\mu^{(i)}$ is a positive step-size selected to minimize the objective along this path. Determining a step-size and search direction at each iteration requires balancing convergence rate with acceptable computational complexity (see [30-32]). The minimization process continues until some prescribed maximum iteration count, or until the relative change in the function value is below a predefined threshold, indicating that a local minimum is found.

V. Simulated Results

A total of $P = 250$ PCFM waveforms were each uniquely initialized with $N = 64$ random and uniformly distributed radial frequency values, generating a collection of RFM waveforms. Each waveform has a pulse width $T = 1.28\mu s$ and is discretized at $F_s = 200MHz$, for a resulting waveform dimensionality of $M = 256$. The maximum permitted phase-change is set to $\Delta_{\phi} = \pi/4$, corresponding to a frequency oversampling of 4, so each PCFM parameter is accordingly bounded between $\pm\pi$. The waveform set is optimized jointly using the approach outlined above, leveraging the quasi-Newton based L-BFGS optimizer [32], with stopping criteria set to a maximum of 10^5 iterations, an objective tolerance of 10^{-9}, and $\wp = 2$. The initial waveforms correspond to the PSF depicted in Fig 1. Because every waveform is unique, the distinct range-sidelobes across slow-time incur the observed RSM pedestal that spreads energy across all Doppler.

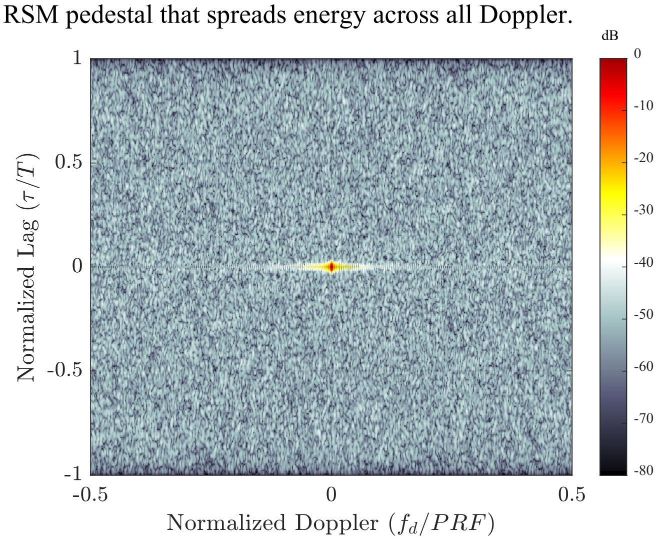

Fig 1. PSF resulting from initial PCFM waveforms

To highlight the design potential for this approach, two different sidelobe regions are considered. The first design (see Fig. 2) selects Ω_{SL} to inscribe the lettering 'KU' in the delay-Doppler plane. The inscription is defined at positive delays and positive/negative Doppler, which therefore becomes reflected at negative delays and negative/positive Doppler, respectively, highlighting the conjugate symmetric relationship of (16). Comparing Fig 1 and Fig. 2, the former represents an uninformed design, while the latter illustrates precise delay-Doppler sidelobe control.

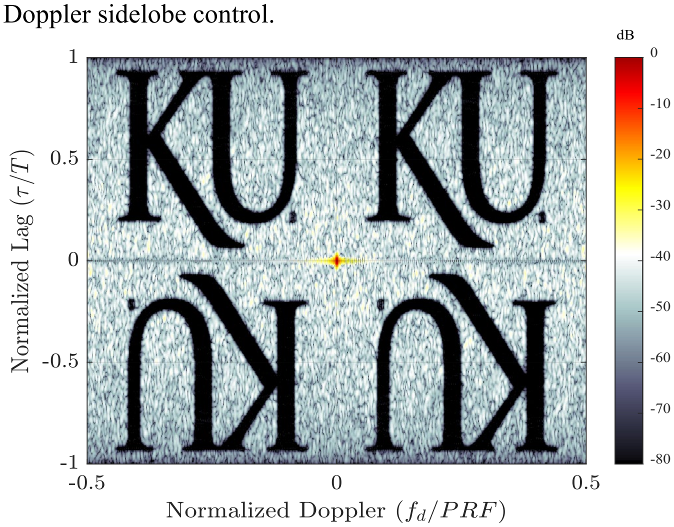

Fig. 2. PSF resulting from jointly optimized PCFM waveforms, with Ω_{SL} selected to inscribe the lettering 'KU' (not useful, but illustrates precise delay/Doppler ambiguity control)

Now consider the case of Ω_{SL} comprising all delay (excluding the mainlobe resolution width) and a band of Doppler associated with radial shifts of $|\theta| \le \pi/2$, as shown in Fig. 3. Here, the set of jointly designed waveforms combine in the PSF to establish a complementary cancellation condition, akin to [15]. Now, the sidelobe energy within the prescribed Ω_{SL} has been largely relocated to outside the desired interval (i.e., to $|\theta| > \pi/2$). Consequently, a notional cognitive mode could conceivably shape the PSF as needed if sufficient knowledge of the scattering environment were available.

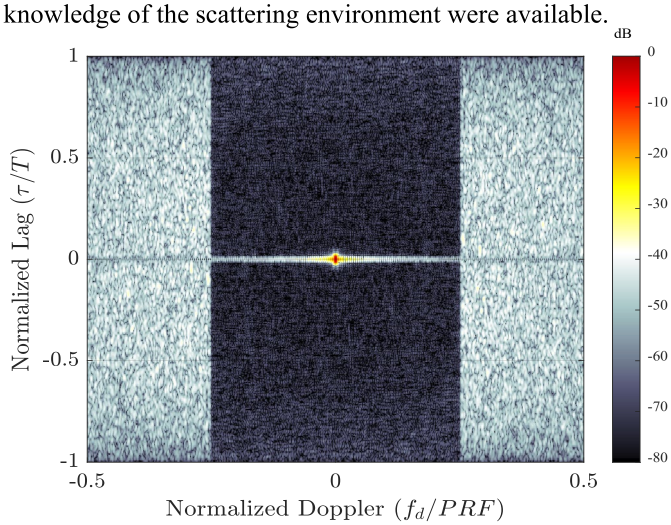

Fig. 3. PSF resulting from jointly optimized PCFM waveforms, with Ω_{SL} selected for all delay and Doppler $|\theta| \le \pi/2$

The average PSDs of the initial and optimized waveforms are shown in Fig. 4, where the optimized set remains largely unchanged (in aggregate) from the initial waveforms. The RMS bandwidth calculated from (10) represents an expansion of only 2.8%, imparted by the slightly higher (~1 dB) power measured at the maximum frequency, which corresponds to the highest weight in (4). This result is in part due to the phase transition limitation from (11), which is confirmed in Fig. 5 where the instantaneous phase-change expands to (but remains contained in) the set limits of $\pm\pi/4$. Indeed, since N was selected to approximate the desired time-bandwidth (with appropriate phase-change limits), a spectral constraint is not necessary during the optimization process for generating these waveforms.

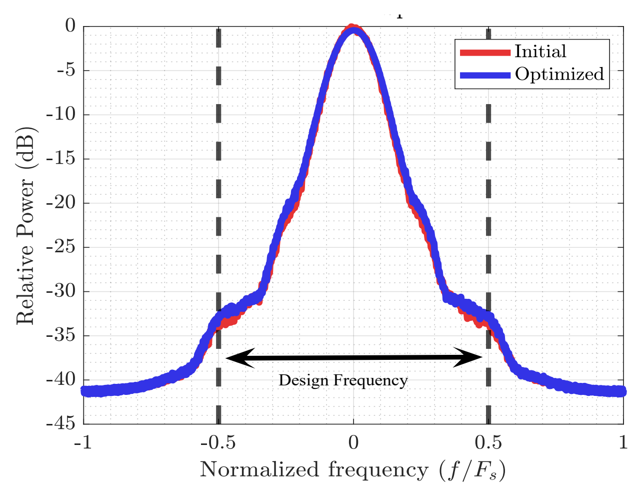

Fig. 4. Mean power-spectra of initial and optimized waveforms

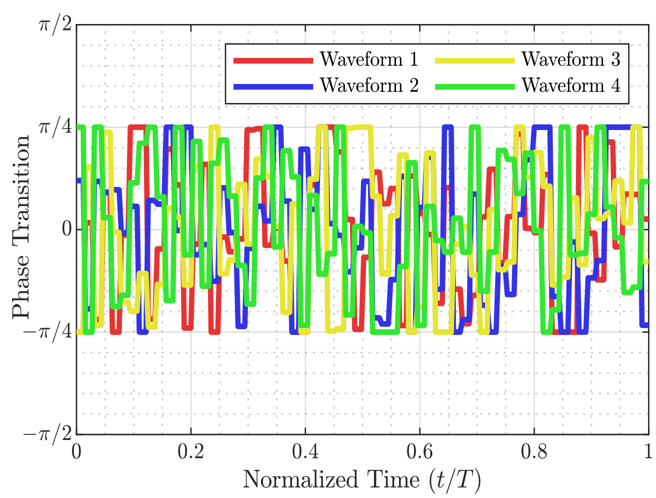

Fig. 5. Instantaneous phase-change of randomly-selected optimized PCFM waveforms

Examination of (20) as a function of gradient-descent iterations reveals a monotonic decrease in total sidelobe energy (see Fig. 6). The optimization is nearly converged after 10^3 iterations, suppressing the ISL by 17 dB, with the remaining 74×10^3 iterations improving by an additional 3 dB until a stopping criterion is met. While unique initializations and selections of Ω_{SL} lead to distinct solutions, this overall trend is consistent across all cases, with most functional decrease occurring rapidly within the initial iterations.

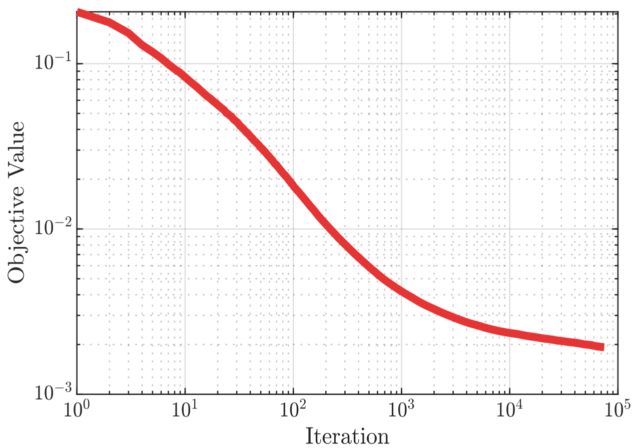

Fig. 6. Objective function value vs iteration index; for case of Ω_{SL} selected for all delay and Doppler $|\theta| \leq \pi/2$

VI. Open-Air Results

To validate practical design amenability, the same three $P = 250$ randomly-initialized and optimized waveform sets were transmitted in an open-air environment consisting of multiple moving vehicles. The waveforms were up-converted to a center-frequency of $f_c = 3.35$ GHz and emitted at a pulse-repetition frequency of PRF = 2 kHz. On receive, the signals were pulse-compressed with the matched-filter, followed by DFT processing in slow-time. To enable adequate comparison between the range-Doppler responses, the three CPIs were concatenated into a single emission, thereby measuring nearly identical scenes from case to case.

First, consider the open-air range-Doppler response from the initial random FM waveforms (Fig. 7), in which the dominant RSM from stationary clutter dominates much of the visible scene, especially at low range due to direct-path leakage from transmitter to receiver. Recall that traditional clutter-cancellation techniques lack the degrees-of-freedom necessary to sufficiently suppress RSM.

Now examine (Fig. 8) the open-air range-Doppler response resulting from the optimized FM waveforms in Fig. 2, which illustrates precise control of the PSF. Clearly, the range-Doppler spread of energy in this case is not conducive to uncover movers, but the inscribed 'KU' that arises from standard pulse compression and Doppler processing highlights the potential for precise control via waveform optimization.

Finally, the response in Fig. 9 is obtained from the optimized FM waveforms of Fig. 3, which provides practical utility by pushing sidelobe energy outside the Doppler band of interest. Here, the impact of clutter is greatly reduced, with many small movers being revealed, while only standard pulse compression and Doppler processing are employed.

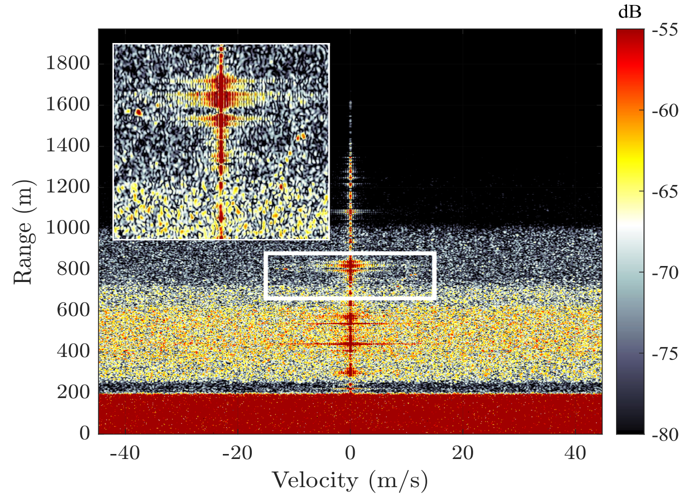

Fig. 7. Range-Doppler response of initial random FM waveforms, with zoomed inset highlighting the location of movers

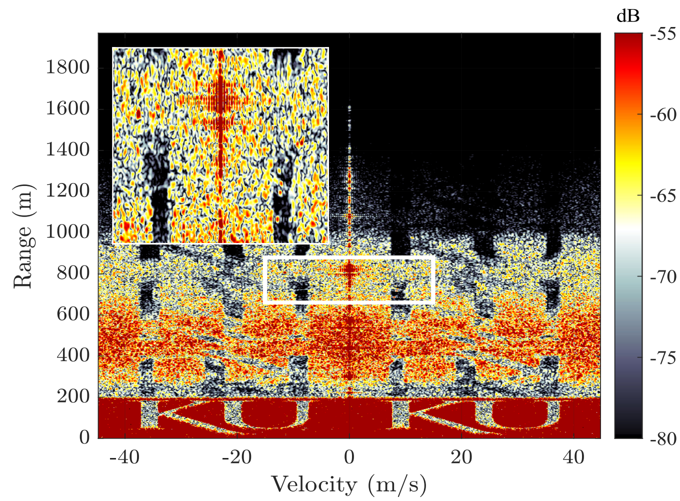

Fig. 8. Range-Doppler response of optimized waveforms, for Ω_{SL} selected to inscribe the lettering 'KU'

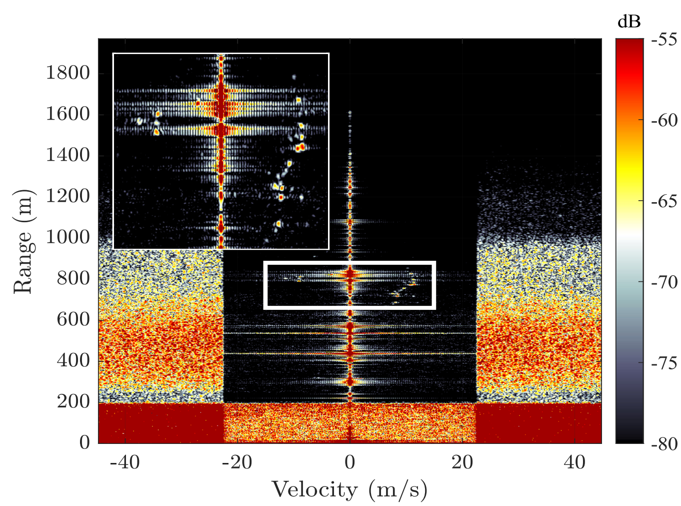

Fig. 9. Range-Doppler response of optimized waveforms, for Ω_{SL} selected for all delay and Doppler $|\theta| \leq \pi/2$

VII. Conclusions

The joint optimization of a set of random FM waveforms is developed to precisely control the delay-Doppler sidelobes of the point-spread function (PSF). Gradient-based minimization of a delay-Doppler GISL objective function enables shaping the range sidelobe modulation (RSM) that results from using non-repeating pulses. The approach subsumes the previously demonstrated Doppler-generalized complementary-FM [15], enabling robust sidelobe suppression in the presence of slow-time Doppler. With sufficient scattering environment knowledge, such an approach could conceivably enable new cognitive implementations. Simulated results are shown to provide precise control of RSM, which is in turn confirmed through open-air experimentation.

References

[1] A.W. Rihaczek, "Doppler-tolerant signal waveforms," *Proc. IEEE*, vol. 54, no. 6, pp. 849-857, June 1966.

[2] J. Klauder, A. Price, S. Darlington, W. Albersheim, "The theory and design of chirp radars," *The Bell System Technical Journal*, vol. 39, no. 4, pp. 745-808, July 1960.

[3] J.W. Owen, C.C. Jones, P. McCormick, D.G. Felton, M.B. Heintzelman, J.E. Quirk, S.D. Blunt, "Analysis of spectrally efficient random FM radar waveforms," *IEEE Intl. Radar Conference*, Rennes, France, Oct. 2024.

[4] S.D. Blunt, et al., "Principles and applications of random FM radar waveform design," *IEEE Aerospace and Electronic Systems Mag.,* vol. 35, no. 10, pp. 20-28, Oct. 2020.

[5] N. Levanon, E. Mozeson, *Radar Signals*, Wiley-IEEE Press, 2004.

[6] Z. Liu, L. Ren, Y. Sun, H. Fan, E. Mao, "Waveform design of LFM pulse train based on pulse width agility," *IET Intl. Radar Conference,* virtual, Nov. 2020.

[7] B. Ravenscroft, J. Owen, J. Jakabosky, S. Blunt, A. Martone, K. Sherbondy, "Experimental demonstration and analysis of cognitive spectrum sensing and notching for radar," *IET Radar, Sonar, & Navigation*, vol. 12, no. 12, pp. 1466-1475, Dec. 2018.

[8] D. Henke, P. McCormick, S. D. Blunt, T. Higgins, "Practical aspects of optimal mismatch filtering and adaptive pulse compression for FM waveforms," *IEEE Intl. Radar Conf.*, Arlington, VA, May 2015.

[9] C.C. Jones, S.D. Blunt, "Mismatched complementary-on-receive filtering of diverse FM waveform subsets," *Intl. Radar Conf.*, Toulon, France, Sept. 2019.

[10] C.C. Jones, *et al*., "Computationally efficient joint-domain clutter cancellation for waveform-agile radar," *IEEE Radar Conf.*, virtual, May 2021.

[11] C.A. Mohr, P.M. McCormick, C.A. Topliff, S.D. Blunt, J.M. Baden, "Gradient-based optimization of PCFM radar waveforms," *IEEE Trans. Aerospace & Electronic Systems*, vol. 57, no. 2, pp. 935-956, Apr. 2021.

[12] D.B. Herr, P.S. Raju, J.M. Stiles, "Information theoretic waveform design with applications to adaptive-on-transmit radar," *IET Radar, Sonar & Navigation*, Oct. 2023.

[13] D.A. Hague, "Adaptive transmit waveform design using multitone sinusoidal FM," *IEEE Trans. Aerospace & Electronic Systems*, vol. 57, no. 2, pp. 1274-1287, Apr. 2021.

[14] A. Farina, A. De Maio, S. Haykin, *The Impact of Cognition on Radar Technology*, SciTech Publishing, 2017.

[15] D.G. Felton, J.W. Owen, M.B. Heintzelman, D.B. Herr, S.D. Blunt, "Improving Doppler robustness for optimized complementary FM waveform subsets," *Intl. Radar Conference*, Rennes, France, Oct. 2024.

[16] J.R. Guerci, E.J. Baranoski, "Knowledge-aided adaptive radar at DARPA: an overview," *IEEE Signal Proc. Magazine*, vol. 23, no. 1, pp. 41-50, Jan. 2006.

[17] A. Aubry, A. De Maio, B. Jiang, S. Zhang, "Ambiguity function shaping for cognitive radar via complex quartic optimization," *IEEE Trans. Signal Processing*, vol. 61, no. 22, pp. 5603-5619, Nov. 2013.

[18] R.A. Scholtz, "How do you define bandwidth?" *Intl. Telemetering Conf.*, Los Angeles, CA, Oct. 1972

[19] D. Gabor, "Theory of communication," *Journal of the IEE,* vol 93, pp. 1946.

[20] L.M. Fink, "Relations between the spectrum and instantaneous frequency of a signal," *Problemy Peredachi Informatsii*, vol. 2, no. 4, pp. 26–38, 1966.

[21] L. Cohen, *Time-Frequency Analysis*, ser. Electrical engineering signal processing. Prentice Hall PTR, 1995.

[22] J. Roberts, "Angle modulation: the theory of system assessment," *IEE Telecommunications Series*. Jan. 1977.

[23] B. White, M.B. Heintzelman, S.D. Blunt, "Alternative 'bases' for gradient-based optimization of parameterized FM radar waveforms," *IEEE Radar Conf.*, San Antonio, TX, May 2023.

[24] S.D. Blunt, M. Cook, J. Jakabosky, J. De Graaf, E. Perrins, "Polyphase-coded FM radar waveforms, part I: implementation," *IEEE Trans. Aerospace & Electronic Systems*, vol. 50, no. 3, pp. 2218-2229, July 2014.

[25] J. Jakabosky, S.D. Blunt, B. Himed, "Optimization of 'over-coded' radar waveforms," *IEEE Radar Conf.*, Cincinnati, OH, May 2014.

[26] P.M. McCormick, S.D. Blunt, "Nonlinear conjugate gradient optimization of polyphase-coded FM radar waveforms," *IEEE Radar Conf.*, Seattle, WA, USA, 2017

[27] A.W. Rihaczek, Principles of High-Resolution Radar, McGraw-Hill, 1969.

[28] S.D. Blunt, E.L. Mokole, "Overview of radar waveform diversity" *IEEE Aerospace and Electronic Systems Mag.,* vol. 31, pp. 2-42, Nov. 2016.

[29] M.A. Richards, *Fundamentals of Radar Signal Processing* (2^{nd} ed.), McGraw-Hill, 2014.

[30] J. Nocedal, S. Wright. *Numerical Optimization*, Springer Science & Business Media, 2006.

[31] W.W. Hager, H. Zhang, "A survey of nonlinear conjugate gradient methods," *Pacific Journal of Optimization*, vol. 2, no. 1, pp. 35-58, Dec. 2005.

[32] N. Vervliet, O. Debals, L. Sorber, M. Van Barel, L. De Lathauwer, Tensorlab 3.0, https://www.tensorlab.net/, Mar. 2016.